Vortex-field enhancement through high-threshold geometric metasurface

Qingsong Wang[1,2†], Yao Fang[1,2†], Yu Meng[1,2], Han Hao[1,2,3], Xiong Li[1,2,3]*, Mingbo Pu[1,2,3,4], Xiaoliang Ma[1,2,3] and Xiangang Luo[1,2,3]*

[1]National Key Laboratory of Optical Field Manipulation Science and Technology, Chinese Academy of Sciences, Chengdu 610209, China; [2]State Key Laboratory of Optical Technologies on Nano-Fabrication and Micro-Engineering, Institute of Optics and Electronics, Chinese Academy of Sciences, Chengdu 610209, China; [3]College of Materials Science and Opto-Electronic Technology, University of Chinese Academy of Sciences, Beijing 100049, China; [4]Research Center on Vector Optical Fields, Institute of Optics and Electronics, Chinese Academy of Sciences, Chengdu 610209, China.

[†]These authors contributed equally to this work.

*Correspondence: X Li, E-mail: lixiong@ioe.ac.cn; XG Luo, E-mail: lxg@ioe.ac.cn

This file includes:

Supplementary information for this paper is available at https://doi.org/10.29026/oea.2024.240112

Section 1: Numerical simulation of the intensity distribution modulated by a sliced phase pattern in the azimuthal direction

During designing a metasurface with the concept of a sliced phase pattern, the initial phase delay between adjacent apertures is an important factor that influences the intensity distribution and intensity gain. Figure S1 shows the phase profile and intensity distribution for initial phase delays $\beta_1=2\pi$ and $\beta_2=\pi$ in the case of a sliced phase pattern featuring 3 sets of angular apertures and one-fold rotational symmetry. Two hot spots in the intensity profile can be generated [Fig. S1(b)], which is different from the intensity profile obtained with $\beta_1=0$ and $\beta_2=0$, as depicted in Fig. 2(d). As a result, lower intensity gain is identified.
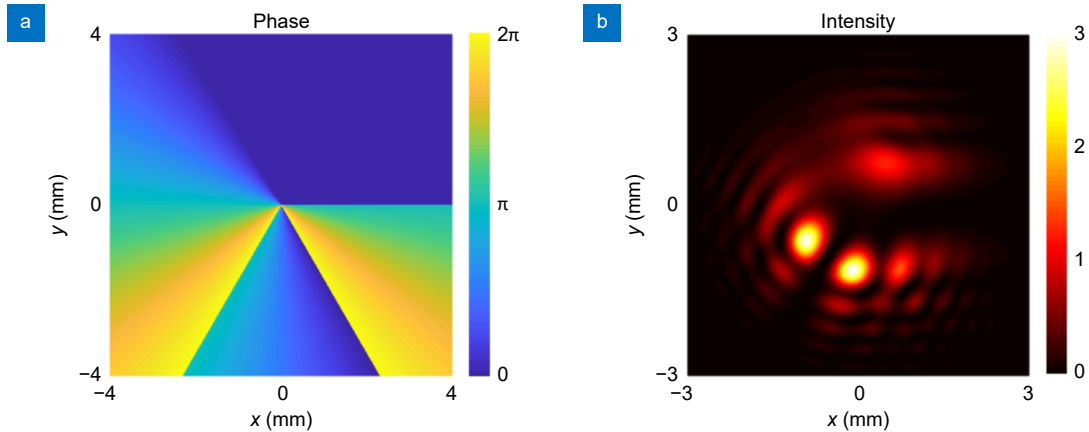
Fig. S1 | Phase profile and intensity distribution for $\beta_1=2\pi$ and $\beta_2=\pi$. The intensity distribution was calculated at a distance of 1 m. The intensity gain is lower than that shown in Fig. 2(b) due to the generation of two hot spots in the intensity profile.

To further demonstrate the concept of a sliced phase pattern, the vortex fields modulated by different sliced phase patterns and laser wavelengths were simulated. Figure S2 shows the simulation results for sliced phase patterns with two sets of angular transmission apertures and two-fold rotational symmetry. The azimuthal phase distribution (φ) can be thus represented as:

$$\varphi\left(\alpha\right) = \begin{cases} l_1\alpha + \theta & \text{Region I} \\ l_2\alpha & \text{Region II} \end{cases}, \tag{S1}$$

where α is the azimuthal angle, l_1 and l_2 are the topological charges in regions I and II, respectively, θ is the initial phase delay between adjacent apertures. The propagation distance is 1 m, and the simulated wavelength is 808 nm. Based on the theory of MCVBs generation using a sliced phase pattern, different topological charges result in different sets of OAM components, leading to varied intensity distributions and intensity gains. Moreover, the change of initial phase delay can influence the spatial-variant interference effect, which also leads to varied intensity distributions and intensity gains. Therefore, the intensity gain changes significantly with different topological charges and initial phase delays, as shown in Fig. S2(b).

In addition, the evolution of the intensity gain on the combination of topological charges and initial phase delays is investigated for a sliced phase pattern featuring 3 sets of angular apertures and one-fold rotational symmetry. The azimuthal phase distribution is detailed in the manuscript [Eq. (1)]. Figure S3 shows the intensity gain as a function of the initial phase delays; the topological charges in regions 1, 2, and 3 are $l_1=0$, $l_2=2$, and $l_3=-2$, respectively. The intensity gain is higher than that in Fig. S2(b), but smaller than that obtained in Fig. 2(a). The main reason is still the generation of different MCVBs, which modulate the creation of optical hot spots with enhanced intensities.

Furthermore, the designed sliced phase patterns can also be applied to enhance the optical intensity for other laser wavelengths. Figure S4 shows the modulated intensity distributions along the propagation direction for wavelengths of 633 nm and 532 nm. The sliced phase patterns are the same as that in Fig. 2(b). The intensity distributions for 808 nm [Fig. 2(e)], 633 nm, and 532 nm are very similar. There is a slight difference in the intensity gain, which may be mainly
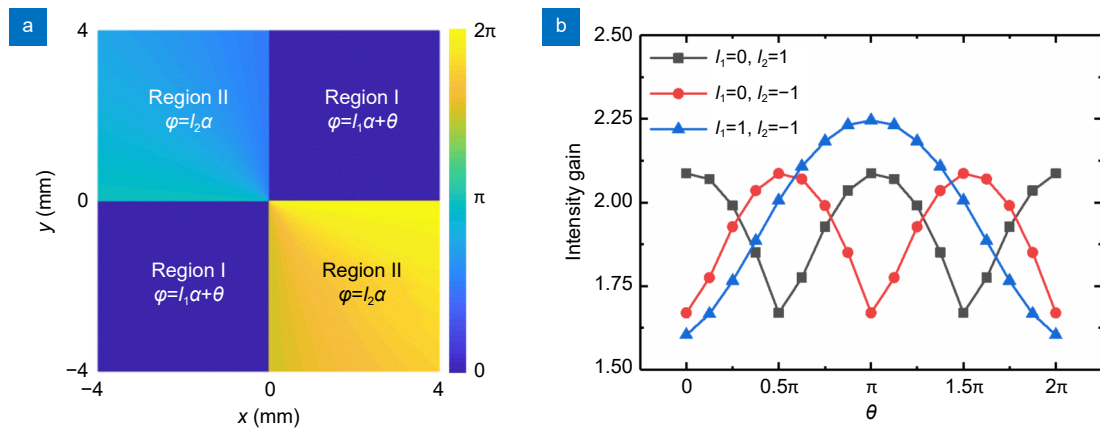
Fig. S2 | Simulation results of intensity gain for sliced phase patterns. (**a**) Schematic diagram of the metasurface phase for a sliced phase pattern with two sets of angular transmission apertures and two-fold rotational symmetry. (**b**) Simulated intensity gains for different combinations of topological charges and initial phase delays.
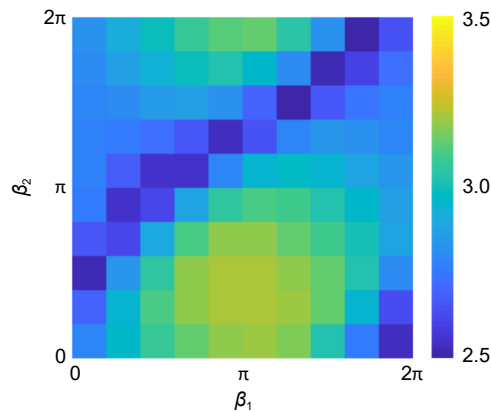
Fig. S3 | Evolution of intensity gain at *z*=1 m with respect to the initial phase delays β_1 and β_2. The topological charges are $l_1=0$, $l_2=2$, and $l_3=-2$ in regions 1, 2, and 3, respectively.
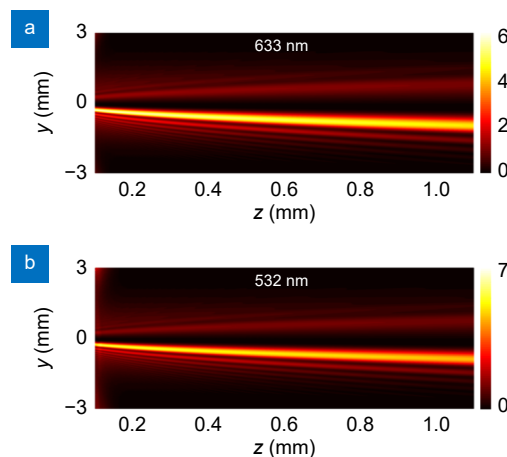

Fig. S4 | Intensity distribution along the propagation direction. The sliced phase patterns are the same as that in Fig. 2(b). The intensity distribution is normalized to the maximum intensity of the Gaussian beam along the propagation direction.

due to the different properties of beam divergence.

It is worth noting that there are a variety of sliced phase patterns with different combinations of varied topological charges and initial phase delays. The aforementioned simulation results are solely examples for illustrating the concept of sliced phase pattern. Innovative works on optimization algorithms would be beneficial to find the proper sliced phase pattern for maximizing the intensity gain at specific distance and wavelength.

## Section 2: The experimental setup for femtosecond laser-induced form birefringence inside silica glass
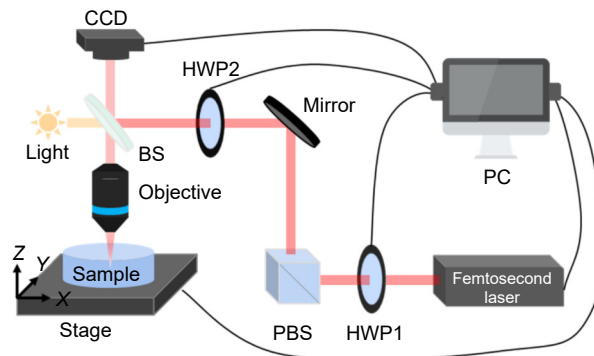
Fig. S5 | Schematic of the experimental setup for femtosecond laser-induced form birefringence inside silica glass. HWP: half-wave plate, PBS: polarizing beamsplitting cube, BS: beamsplitter. CCD: charge coupled device.

Section 3: Absorption spectra of type I, type II, and type X modifications
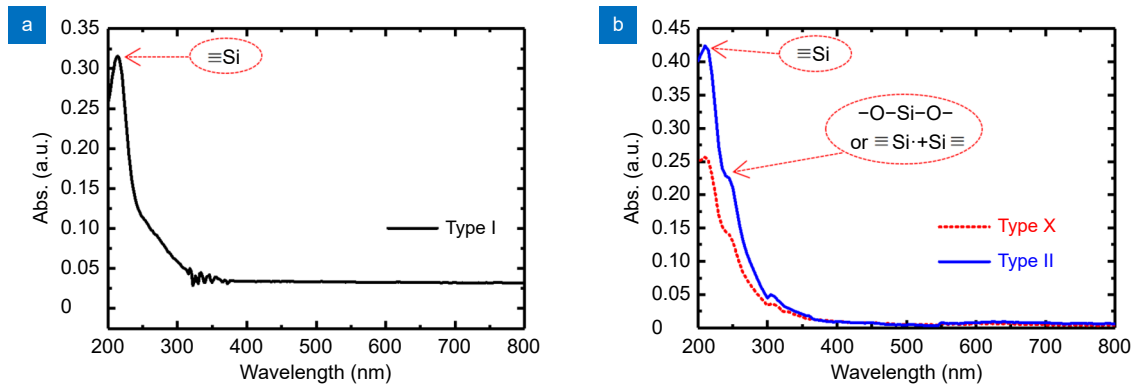

Fig. S6 | Absorption spectra of type I, type II, and type X modifications. Laser-induced defects can be identified according to the absorption spectra.

## Section 4: Morphology characterization of laser-induced form birefringence
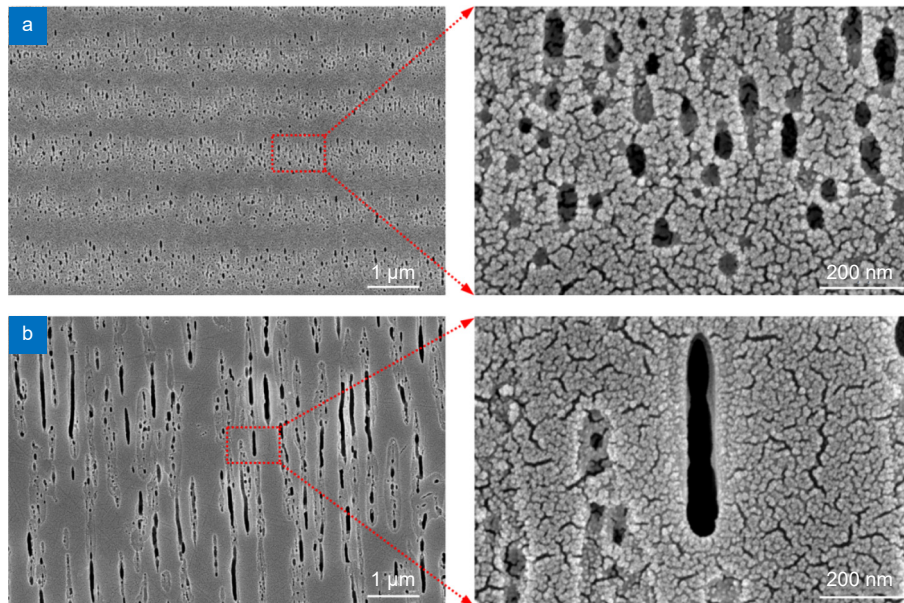
Fig. S7 | SEM images of laser-induced form birefringence. (**a**) Laser-induced type X modification with laser parameters of 450 fs pulse duration, 33 pulses/μm pulse density, and 1.1 μJ pulse energy. (**b**) Laser-induced type II modification with laser parameters of 450 fs pulse duration, 200 pulses/μm pulse density, and 1.1 μJ pulse energy. Smaller feature size is characterized in type X modification.

Section 5: Dependence of retardance on the interval-distance of layers and polarization direction
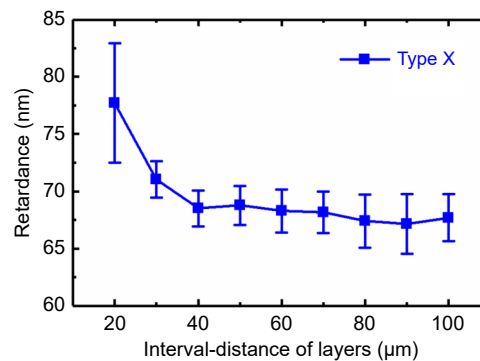
Fig. S8 | Dependence of retardance of three-layer type X modification on interval-distance of layers. Laser parameters of 450 fs pulse duration, 33 pulses/μm pulse density, and 1.1 μJ pulse energy are employed.
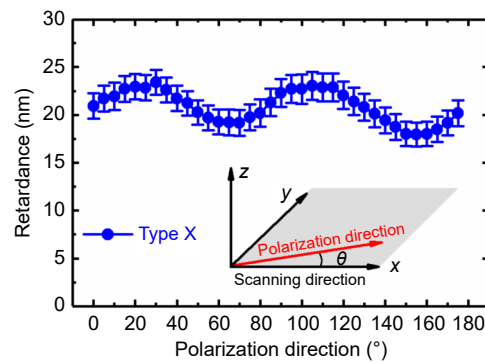
Fig. S9 | Dependence of retardance for type X modification on the polarization direction of femtosecond laser with respect to the laser scanning direction. Single-layer type X modification is generated with varied femtosecond laser polarization direction. The laser scanning direction is along the *x*-axis direction. Laser parameters of 450 fs pulse duration, 33 pulses/μm pulse density, and 1.1 μJ pulse energy are employed.

Section 6: The parameters involved in the fabrication of type II and type X metasurfaces

Table S1 | The parameters involved in the fabrication of type II and type X metasurfaces.

Parameter	Type II metasurface	Type X metasurface
Laser central wavelength	1030 nm	1030 nm
Repetition rate	205 kHz	205 kHz
Objective	10×, *NA* = 0.26	10×, *NA* = 0.26
Pulse duration	450 fs	450 fs
Pulse energy	1.1 μJ	1.1 μJ
Pulse density	200 pulses/μm	33 pulses/μm
Number of layers	4	20
Interval distance of layers	40 μm	40 μm

Section 7: Cross-sections of the modulated optical patterns
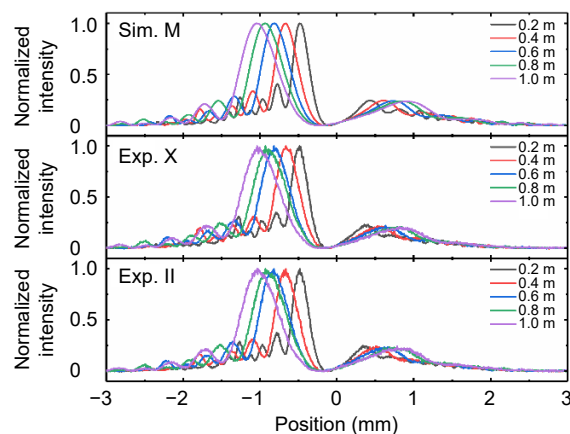
Fig. S10 | Normalized intensity along the dashed lines indicated in Fig. 5(a) for the simulated and measured optical patterns acquired at different propagation distances.